Desalination 525 (2022) 115493

Contents lists available at ScienceDirect

Desalination

journal homepage: www.elsevier.com/locate/desal

Predicting capacitive deionization processes using an electrolytic-capacitor (ELC) model: 2D dynamics, leakages, and multi-ion solutions

Johan Nordstrand [a], Léa Zuili [a], Esteban Alejandro Toledo-Carrillo [a], Joydeep Dutta [a,b,*]

[a] Functional Materials Group, Applied Physics Department, School of Engineering Sciences, KTH Royal Institute of Technology, AlbaNova universitetscentrum, 106 91 Stockholm, Sweden
[b] Center of Nanotechnology, KingAbdulaziz University, Jeddah 21589, SaudiArabia

HIGHLIGHTS

- ELC model blends battery modeling and key concepts in capacitive deionization (CDI).
- Two-dimensional (2D) simulation of adsorption and ion transport during desalination
- Tractably models desalination, Faradaic leakage reactions, and multi-ion solutions.
- Simulations with ELC are generally applicable and scalable to features.
- The manuscript offers COMSOL integration for easy model implementation.

ARTICLE INFO

Keywords:
Capacitive deionization
Desalination
Modeling
Electrolytic capacitor
Comsol
Simulation

ABSTRACT

Clean water and affordable energy are critical worldwide challenges for which electrolytic capacitors are increasingly considered as viable alternatives. The upcoming technology of capacitive deionization (CDI) uses similar electrolytic capacitors for the desalination of water. The current work presents a new method that leverages existing support for supercapacitors in the form of current-distribution models, which enables detailed and separated descriptions of the rate-limiting resistances. Crucially, the new model blends this basis with a novel formulation centered on the adsorption of chemical species in CDI. Put together, it is adaptable to solving a wide range of problems related to chemical species in electrochemical cells. The resulting electrolytic-capacitor (ELC) model has enhanced stability and ease-of-implementation for simulations in 2D. The results demonstrate that the model accurately simulates dynamics CDI performance under a variety of operational conditions. The enhanced stability together with the adaptability further allows tractable simulations of leakage reactions and even handling multi-ion deionization in 2D. Moreover, the model naturally blends with existing interfaces in COMSOL Multiphysics, which automatically generalizes, stabilizes, and simplifies the implementation. In conclusion, the ELC model is user-friendly and tractable for standard simulations while also being especially powerful when simulating complex structures, leakage reactions, and multi-ion solutions.

1. Introduction

Affordable fresh water and energy are crucial components for meeting the future world challenges [1–3] and are central to achieving the UN sustainability goals [4–6]. Porous electrolytic capacitors are used for batteries [7], energy production from salinity differences (blue energy) [8–15], and capacitive water purification [16]. Specifically, capacitive deionization (CDI) [16–19] is an upcoming desalination technique that works like an electrolytic capacitor. Highly porous electrodes are placed close to each other and separated by a thin spacer in CDI devices, similar to capacitors (Fig. 1) [20]. During the charging process, ions in the electrolyte accumulate in electric double layers on the electrodes similar to a typical electrolytic capacitor [7]. However, instead of storing energy, the purpose is to use a passing salty water stream as an electrolyte, so that electro-adsorbing the ions in the electrodes leads to the production of desalinated water [16]. Electrode

Abbreviations: CDI, Capacitive Deionization; ELC, Electrolytic Capacitor.

* Corresponding author.
E-mail address: joydeep@kth.se (J. Dutta).

https://doi.org/10.1016/j.desal.2021.115493
Received 16 August 2021; Received in revised form 26 November 2021; Accepted 3 December 2021
Available online 21 December 2021

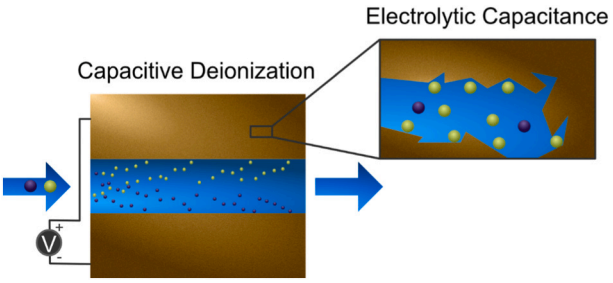

Fig. 1. Device design in capacitive deionization. The CDI unit is comprised of two porous electrodes separated by a non-conducting spacer. During the desalination process, an applied voltage drives ions from the passing water stream to migrate to the porous electrodes and adsorb. Enlargement: Like an electrolytic capacitor, the CDI electrode gets a huge capacitance and thus adsorption from the electrode-electrolyte interaction in the porous matrix. However, features such as the expulsion of co-ions lead to distinct differences between capacitance and adsorption capacity, thus necessitating CDI-specific modeling approaches.

materials [21,22,31–36,23–30] and operational [37–41] conditions influence the effectiveness of this process, so modeling can be crucial for optimizing cell designs, scaling systems, and efficient operation.

Because designing supercapacitor systems have been important for a long time, researchers have developed extensive theoretical frameworks for describing these processes, and COMSOL Multiphysics has incorporated many of these formulations into its core libraries [42]. Having this extensive integrated support for electrolytic capacitors makes it fundamentally natural to use them for CDI as well, but this is typically not the case today. Rather, a variety of alternative approaches have been developed including the modified Donnan (mD) model [16,17,20,21,43,44], the dynamic Langmuir (DL) model [45–52], and circuit-based models [28,53–55], amongst others. While many researchers have utilized the COMSOL platform [20,21,29,33,43,44,56–59], they typically use custom homebrew interfaces that are limited in scope, stability, and scalability.

In this work, we leverage the strength of existing theory for supercapacitors in the form of Current Distribution Interfaces in COMSOL [42] to create an electrolytic-capacitor (ELC) model specifically adapted to the adsorption of chemical species in CDI. There are distinct similarities between some modern CDI modeling approaches (e.g., the mD model) and supercapacitor modeling, but the result section will reveal that a supercapacitor-based model can obtain accurate simulations with enhanced stability and more tractable implementations. However, there are also distinct differences between the standard electrolytic capacitor and the CDI device, so we derive a theoretical formulation that addresses the issues that are core to CDI operations.

2. Theory

2.1. Goals

Before introducing the model, let us discuss the goal and criteria of the model development. The goal of this work is to derive a broad model that enhances numerical stability and facilitates straightforward implementation. The model should also obtain at least as good accuracy as earlier models.

The stability goal will be pursued through innovations in theory and numerical methods. Firstly, fewer and less interconnected PDE structures should be developed to describe the model structure. The basis for FEM calculations is that all provided equations must hold at all time steps. Thus, large sets of convoluted equations will naturally increase the difficulty any program has when simulating the system. Secondly, the model development should see to reduce the severe nonlinearities compared to existing models. Severe nonlinearities mean that small changes in conditions can lead to large errors, which is the typical reason that FEM calculations fail to converge. Thirdly, the differential equation will be preferred over quasi-equilibrium conditions. Such equations will provide direct information about how the system evolves, rather than imposing implicit constraints that must always be kept.

The implementation goal will be pursued through generality, flexibility, and shared resources. If the model framework is adaptable, as opposed to tailored to a system, this means that the same mathematical framework could be used in a variety of situations. For instance, in an adaptable model, it would be possible to change the device structure while keeping the physics and get correct simulation results. We will also seek to make the model flexibly through a decoupled model structure; that is, specific parts of the model will be possible to exchange as research progresses in the future, without affecting the rest of the model structure. Lastly, if the developed theory can be framed in a way that is consistent with existing interfaces in the commonly used FEM software, that would greatly simplify the implementation because users would not have to redo the model from scratch. Also, things like internal boundary conditions could be handled automatically, so the user will not have to implement such details by hand.

As a final point, we will leverage the enhanced stability that the new model provides and demonstrate that it can straightforwardly simulate features that normally generate instability in the 2D setting: leakages and multi-ion solutions.

2.2. Electrode current

In the following section, we will introduce formulations that can directly calculate the current and ionic movements inside the device based on the device conditions. To obtain the stability and implementation goal, the initial derivations will mimic the formulation for classic capacitor (battery) systems and the CDI-specific issues will be addressed at a later stage.

The CDI device is similar to an RC circuit where an external voltage V_{ext} drives a charging current i (Eq. (1)). During the charging step, series-resistive losses ($R_c i$) consume some of this potential, while the rest distributes at the boundary of each electrode ($\phi_{s,\,b}$).

$$\phi_{s,b} = \pm (V_{ext} - R_c i)/2 \tag{1}$$

The boundary potential then translates through the conductive electrode, leading to a potential ϕ_s in the electrode matrix that relates to the electrode matrix current $\boldsymbol{i_s}$ through the corresponding conductivity σ_s (Eq. (2)). Models commonly assume the material is highly conductive [20] (high $\sigma_s \rightarrow \phi_s = \pm V_{ext}/2$) but this expression makes it possible to describe materials with varying conductivity. As the cell charges, a localized volumetric current ($i_{v,\,tot}$) passes between the electrode matrix and the electrolyte (saline water), yielding the current continuity in Eq. (3). This volumetric current contributes to the total device current (Eq. (4)) and ultimately affects the total external resistive losses represented in Eq. (1). Note that the derivations use **bold** font to denote vector parameters while normal font corresponds to scalars.

$$\boldsymbol{i_s} = -\sigma_s \nabla \phi_s \tag{2}$$

$$\nabla \cdot \boldsymbol{i_s} = -i_{v,tot} \tag{3}$$

$$i = \iiint_s i_{v,tot}\, dx \tag{4}$$

2.3. Electrolyte current

Moving from electrode to electrolyte, the current in the electrode yields a corresponding current in the liquid ($\boldsymbol{i_l}$, Eq. (5)).

$$\nabla \cdot \boldsymbol{i_l} = i_{v,tot} \tag{5}$$

A CDI cell is fundamentally an electrolytic capacitor, and as such, the

current in the electrolyte inside it is closely linked to the ion flux (Eq. (6)). Here, subscript l indicates electrolyte (liquid), z_i is the valency of species i, F is the Faraday constant, and $\boldsymbol{N_i}$ is the vector ionic flux of species i. The total ionic flux consists of ion diffusion, electromigration, and convection, respectively as shown in Eq. (7). Here, D_i is the bulk diffusion constant of species i, $u_{m,\,i}$ is the mobility, ϕ_l is the electrolyte potential, and $\boldsymbol{u}$ is the vector flowrate. Now, summing all contributions for each ionic species leads to Eq. (8) for describing the current.

$$\boldsymbol{i_l} = F\sum_i z_i \boldsymbol{N_i} \tag{6}$$

$$\boldsymbol{N_i} = -D_i\nabla c_i - z u_{m,i} F c_i \nabla\phi_l + c_i\boldsymbol{u} \tag{7}$$

$$\boldsymbol{i_l} = -F\left(\nabla\sum_i z_i D_i c_i\right) - F^2\nabla\phi_l\sum_i z_i^2 u_{m,i} c_i + \boldsymbol{u}F\sum_i z_i c_i \tag{8}$$

In the bulk electrolyte there is charge neutrality, meaning $\Sigma_i z_i c_i = 0$. We will also presume that the ionic species have similar diffusion coefficients, so $\Sigma_i z_i D_i c_i$ is small and can be neglected. Thus, only the electromigration term contributes significantly to the net current.

The solutions investigated in this work mainly contain two monovalent ions, sodium chloride (NaCl) and potassium chloride (KCl). In these cases, we have $z_+ = 1$ and $z_- = -1$ and charge neutrality implies $c_+ = c_- = c$. Inserting these relations simplifies Eq. (8) into Eq. (9), showing that the current in the liquid is a function of the liquid conductivity (σ_l) and the electric field ($-\nabla\phi_l$). The key point here is that the electrolyte conductivity depends strongly on the ion concentration, which is important when simulating the ion-starved conditions (very low salinity water).

$$\boldsymbol{i_l} = -F^2\left(u_{m,+} + u_{m,-}\right)c\nabla\phi_l = -\sigma_l\nabla\phi_l \tag{9}$$

To calculate the ionic mobility, we use the Nernst-Einstein relationship $u_{m,\,i} = D_i/RT$. Here, R is the gas constant and T is the temperature.

2.4. Charging rate

The previous sections describe how currents move through the electrode matrix and the electrolyte, and in this section, we investigate the charging rate. The total localized current has two components, double-layer charging ($i_{v,\,dl}$) and Faradaic reactions (i_v) (Eq. (10)).

$$i_{v,tot} = i_{v,dl} + i_v \tag{10}$$

By the definition of capacitance, the volumetric double-layer capacitance (C_{dl}) relates the double layer charging rate to how quickly the potential difference between the electrode and electrolyte changes (Eq. (11)). Here, it should be noted that the capacitance is only constant if the ionic concentration is high and it is only approximately constant with the voltage. To stay within the decoupled framework, we will separately include such dependence.

$$i_{dl} = C_{dl}\frac{\partial(\phi_s - \phi_l)}{\partial t} \tag{11}$$

The Butler-Volmer equation states that the rate of Faradaic reactions depends exponentially on the potential (Eq. (12)). Here, i_0 is the volumetric exchange current density, α_a is the anodic transfer coefficient and α_c is the cathodic transfer coefficient. For reasonably small potentials this expression reverts to the linearized form in Eq. (13), making the volumetric current proportional to the potential difference through some leakage resistance R_L at a given temperature (Eq. (14)).

$$i_v = i_0\left(exp\left(\frac{\alpha_a F(\phi_s - \phi_l)}{RT}\right) - exp\left(\frac{-\alpha_c F(\phi_s - \phi_l)}{RT}\right)\right) \tag{12}$$

$$i_v = i_0\frac{(\alpha_a + \alpha_c)F}{RT}(\phi_s - \phi_l) \tag{13}$$

$$i_v = (\phi_s - \phi_l)/R_L \tag{14}$$

2.5. Adsorption rate

The double-layer charging makes ions accumulate in the electrodes, thus removing them from the liquid at a rate R_i (Eq. (15)). Here ν is the stoichiometric coefficient and n is the number of electrons involved in the charging step.

$$R_i = -\frac{\nu i_{v,dl}}{nF} \tag{15}$$

In this work, we mainly investigate solutions with a monovalent anion and a monovalent cation (although the formulations can be readily extended for multi-valent ions). Thus, we will let $\boldsymbol{c}$ denote the total salt concentration with both electrodes contributing to reducing ion concentrations in the liquid. This means $n = 2$ at the cathode and $n = -2$ at the anode (NaCl and KCl contain two charged ions). Moreover, ν thus corresponds to the charge efficiency Λ, and to simplify calculations a representative constant value can be taken for the time-dependent process.

In our earlier work with the dynamic Langmuir (DL) model we derived equations for the dependency of charge efficiency on applied voltage (Eq. (16)) [45]. Here, V_0 is a constant and we will use this expression for predicting the performance under varying applied voltages.

$$\Lambda = 1 - V_0/V_{ext} \tag{16}$$

Note that, in earlier work, the charge efficiency is strongly interconnected with the charging state. This is physically correct but complicates the numerical modeling performance. Instead, the equation above stays within the decoupled and flexible framework. Because the equation is separate from the previous calculations, the added complexity is minor. Also, the formulation here could be exchanged for any other decoupled description for the charge efficiency. For instance, this equation does not describe how the charge efficiency varies with the ionic concentration. However, that dependence could be included by changing the expression to a form like the one presented in ref. [45].

2.6. Ion transport

In regions of free flow, Eq. (17) governs the ionic transport based on diffusion, convection, and reactions, while the Brinkman equations can be used for separately determining the water flow [60]. With this setup there is no limitation on the type of device structure of flow mode; the model handles combinations of convective and diffusive flux.

$$\frac{\partial c_i}{\partial t} + \nabla\cdot\left(-D_i\nabla c_i\right) + \boldsymbol{u}\cdot\nabla c_i = R_i \tag{17}$$

2.7. Effect of porosity

In the porous regions of the electrodes and spacers (porosity ϵ_p), the liquid resides only in part of the electrodes, making the effective volume concentration lower than the actual concentration ($c_{eff,\,i} = \epsilon_p c_i$) (Eq. (18)). Also, the effective diffusion is lower than in the bulk, and the Bruggeman correction accounts for this difference (Eq. (19)). Because diffusion affects ionic mobility, the same correction factor also applies to the ionic conductivity in Eq. (9). The point of using specifically the Bruggeman correction aside from a guess about the effective diffusion (see ref. [20] and the supplementary in ref. [56]) is that it establishes a common framework for investigating models with varying electrode materials.

$$\frac{\partial\left(\epsilon_p c_i\right)}{\partial t} + \nabla\cdot\left(-D_{eff,i}\nabla c_i\right) + \boldsymbol{u}\cdot\nabla c_i = R_i \tag{18}$$

$$D_{eff,i} = \epsilon_p^{3/2} D_i \tag{19}$$

2.8. Multi-ion formulation

Multi-ion modeling is interesting because it adds another layer of interconnectedness to the model. This makes it a promising area for decoupled modeling, such as this work.

In the earlier description of single-ion adsorption (Eq. (15)), a known stoichiometric coefficient of each species would make it possible to directly calculate the adsorption of each species based on the total current. The challenge here is that they are unknown and depend on the charging state of the device as well as the concentrations of all the ionic species. Moreover, variations in bulk concentration can lead to charging as well as discharging of the devices that are missing in Eq. (15). Hence, even the best fitting parameters could only describe capacitive charging but not ion-exchange processes.

The mD model states that the potential difference between the micropore and the macropores uniquely defines the relationship between the adsorbed concentration $c_{m,\,i}$ of each species i and the corresponding bulk concentration $c_{M,\,i}$. This potential consists of Donnan (charging) potential $\Delta\overline{\phi}_D$ and micropore potential $\overline{\mu}_{att,i}$ (passive, material dependent). If the micropore potential is known, the charging state $\Delta\overline{\phi}_D$ determines and Eq. (20) thus defines the adsorption of each ionic species.

$$c_{m,i} = c_{M,i} exp\left(\overline{\mu}_{att,i} - z_i \Delta\overline{\phi}_D\right) \tag{20}$$

This description is physically sound but has numerical issues related to introducing extra quasi-equilibrium constraints, as discussed at the beginning of the theory section. More importantly, COMSOL Multiphysics has set interfaces that can automatically implement the model, as long as the adsorption follows the form in Eq. (15). Amongst other things, using set interfaces simplifies implementation and automatically handles internal boundary conditions, which facilitates scalability to new geometries. To use such frameworks, we must thus derive a formulation that has the same form as Eq. (15).

In this work, we propose an alternative numerical approach to address this. First, setting the stoichiometric coefficient to 1 for one species at each electrode (e.g. Na^+ and Cl^-) and 0 for all other species sets a foundation corresponding to ideal charging for only the species in consideration (Eq. (21): $R_{dl,\,i}$ is 1 for the specified species and zero otherwise) rendering it stable. Then, we introduce an equilibrium reaction $R_{e,\,(i,j)}$ corresponding to fast ion exchanges between two species i and j. Let the excess concentration of species i be e_i (Eq. (22)); that is, the error compared to the actual value in Eq. (20). The formulation for $R_{e,\,(i,\,j)}$ now decreases the adsorption of the species with the most excess concentration and increases the concentration for the species with the lowest excess concentration (Eq. (23)). Note that $z_i R_{e,\,(i,j)} + z_j R_{e,\,(j,i)} = 0$, which means the reaction conserves the total charge in the system as it should.

$$R_{tot,i} = R_{dl,i} + \Sigma_j R_{e,(i,j)} \tag{21}$$

$$e_i = c_{m,i} - c_{M,i} exp\left(\overline{\mu}_{att,i} - z_i \Delta\overline{\phi}_D\right) \tag{22}$$

$$R_{e,(i,j)} = -kz_j\left(z_i e_i - z_j e_j\right) \tag{23}$$

This formulation will set the correct balance between all species throughout the simulated desalination process. By setting the arbitrary reaction constant k large enough, the best exact balance of Eq. (20) holds for all adsorption periods. Notably, for reactions where i and j have the same charge signs, Eq. (23) ensures the most accurate balance between the species. For different charge signs, the same balance also sets the charge efficiency for the entire system. For instance, in a binary electrolyte of Na^+ and Cl^-, the reaction would adsorb/expel both Na^+ and Cl^- until the balance between them is correct at each electrode. This unideal balance corresponds to co-ion expulsion, which affects the charge efficiency.

Initially, it may seem like these equations raise, rather than lower, the complexity of the system. However, the opposite is true. The new formulation stabilizes the system by making the constraint laxer. The reason Eq. (20) is difficult for the program to implement is that it is a harsh implicit constraint that must be met at all time steps. On the contrary, the new formulation records how big the deviation is in the constraint, and it explicitly states how to remove this error in the next time step. Thus, the computation can never fail because of these equations. Crucially, a large value of k will make the errors vanish much faster than the charging timescale in the device, so for all practical purposes, the new formulation exactly enforces Eq. (20) but in a more stable way.

2.9. Boundary conditions

Boundary conditions are a minor concern in the derived model because it is adapted to fit in COMSOL interfaces that will automatically handle internal boundary conditions.

Still, the equations derived in the previous sections require information about the external boundary conditions to make the problem solvable. For the water flow, the closed external boundaries can be considered not to have slip conditions ($u = 0$) while the inlet has a constant flow velocity, and the outlet has zero-pressure conditions. For ion transport, the closed external boundaries have no-flux conditions ($-\boldsymbol{n} \cdot (-D_i \nabla c_i + \boldsymbol{u}c) = 0$, where $\mathbf{n}$ is the normal vector) while the inlet uses a set concentration (c_{in}). Also, the outlet uses zero diffusive flux since the concentration does not change after exiting the cell $-\boldsymbol{n} \cdot (-D_i \nabla c_i)$. For the current and potential, there is no current exiting the external boundaries ($-\boldsymbol{n} \cdot i_s = -\boldsymbol{n} \cdot i_l = 0$) except the areas connected to the external circuit where the potential keeps to the externally set value (Eq. (1)). Overall, the internal boundaries require that all mass flux and current be constant across them.

2.10. Parameter fitting

In the literature, some established models do not present algorithms for extracting fitting parameters, while others (including our previous work) have complicated schemes that can be arduous to implement. Keeping in line with the goal of straightforward implementations, we will here present a pen-and-paper approach to parameter fitting. Notably, it is the earlier groundwork on the model formulation that makes the simple yet effective methods possible.

In previous work on the Donnan model, three fitting parameters were used, including the micropore capacitance C_m, the micropore attraction $\overline{\mu}_{att}$, and the microporosity p_m. Also, the value of the total series resistance R_c and the choice of how the corrected diffusion constant in the porous regions were found to affect the system dynamics. Fundamentally, these parameters correspond to the core degrees of freedom in the CDI system, including total charge-storage capacity, total adsorption, charging rate, and ion-transport responsiveness.

In the current work, we measure the capacitance based on the standard capacitance formulate (Eq. (24), q_e is the equilibrium stored charge). With multiple data points, the same value follows from the linear regression (mean). Note also that the double-layer capacitance is twice the normal capacitance when the cell comprises two identical electrodes ($C_{dl} = q_e/(V_{ext}/2)$). This sets the total charge storage.

$$C = q_e / V_{ext} \tag{24}$$

Following the DL model, the voltage-dependent charge efficiency is considered to follow the threshold voltage V_0 (Eq. (25)). Linear regression can again find the parameter if there are multiple data points where the experimental charge efficiency has been measured. Note that V_0 is simply the place where the linear trend on the charge-voltage graph meets the x-axis. It should be zero if the charge efficiency is high in the

system but will be larger than zero if the charge efficiency is unideal. Because the charge efficiency relates charge to adsorption, this determines the total electro-sorption of ions in the device. Mathematically, we can note that V_0 plays a similar role as $\bar{\mu}_{att}$ in the mD model.

$$V_0 = V_{ext}(1-\Lambda) \tag{25}$$

In previous work it was argued that the contact resistance is responsible for most of the resistive losses during charging, so we calculated R_c resistance as the RC constant in data for the current during non-starved charging. Another simpler option is to just calculate the resistance based on the initial total current and voltage [49] (Eq. (26)).

$$R_c = V_{ext,start}/i_{start} \tag{26}$$

This determines the charging rate. To increase the accuracy in leaky systems, we instead fitted a Randles circuit [49,51] to the total current data from those experiments, which yields the leakage-corrected values for the series resistance and the capacitance (Fig. 2, see derivation in [49,51]).

The microporosity is typically measurable but the effective porosity is not always the same as observed in the experiments. Previous work has tested different porosity values to get the best data fit which sets the ion-transport responsiveness. Scanning different values is possible to do with this method too, although we have used the same value as in previous work for comparison. Mainly, we just used the actual porosity determined from experimental measurements.

Going beyond the core adsorption model, the current leakages primarily occur after a long period of charging (i_e, equilibrium current). Ultimately, there can be no adsorption at equilibrium, so all current is due to leaked charges at that point. This also means the leakage resistance directly follows from the experimentally measured current (Eq. (27)).

$$R_L = i_e/\left(\phi_{s,e} - \phi_{l,e}\right) = i_e/(V_{ext}/2) \tag{27}$$

For the multi-ion formulation, summing Eq. (20) for both electrodes (assuming equal Donnan potentials) leads to a closed expression for the net adsorption of individual ions (Eq. (28)). Also, summing the valency-weighted total adsorption for all ions leads to the net total charge (Eq. (29)). Because the number of equations is the same as the number of unknown parameters, a nonlinear solver can find the values for the fitting parameters from equilibrium-adsorption data for any number of species. In the equations, Γ_i is the net adsorption of species i (unit mM), Q is the total charge storage (unit C) with the equilibrium bulk concentration of species i, F is the Faraday constant, p_m is the microporosity, and V_e is the total volume of one electrode (see Ref. [20] for comparison).

$$\Gamma_i = 2c_{0,i}exp\left(\bar{\mu}_{att,i}\right)(cosh(z_i\Delta\bar{\phi}_D) - 1)p_m V_e \tag{28}$$

$$Q = \Sigma_i 2Fz_i c_{0,i} exp\left(\bar{\mu}_{att,i}\right) sinh(z_i\Delta\bar{\phi}_D) p_m V_e \tag{29}$$

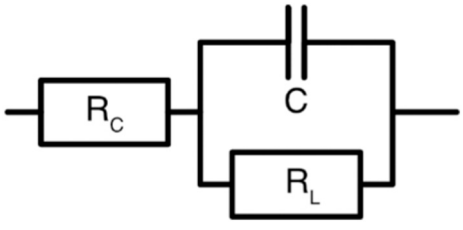

Fig. 2. Schematic representation of a typical CDI system as a Randles circuit. The cell is fundamentally a capacitor with capacitance C that determines the total charge-storage capacity. Leakage currents pass through the cell rather than accumulating on the capacitor, as determined by the leakage resistance R_L. Finally, the series resistance R_c determines the speed of the charging process. This 0D model is especially relevant when analyzing the leakage trends that the ELC model predicts.

As a side note, it is also possible to use a system-identification method to derive all parameters based on time-series data instead of the equilibrium data (Supplementary Section 4).

3. Methods

3.1. Implementation

COMSOL Multiphysics 5.5 was used for all the simulations based on the derived theory where the Brinkman equations interface was applied to simulate the background flow. In the basic model, the interface for the secondary current distribution (with the porous electrode) computes the currents, while the interface for transport of diluted species in porous media (with porous electrode coupling) can be used for simulating the ion adsorption and transport. In the advanced model, the tertiary current distribution was used to simulate both the current and the ion transport.

3.2. Experiments from the literature

To investigate the tractability of this new model formulation we compared it to the seminal work of Hemmatifar et al. [20], wherein the authors developed the first complete two-dimensional model for investigating CDI performances. The mD model in this work was developed considering their device and experimental conditions. The CDI device described by Hemmatifar et al., structurally looks like the top device in Fig. 1, using an elongated design with an air-gap spacer so that the water freely flows between the electrodes from the inlet to the outlet pipe. Their electrode material was activated carbon cloth (ACC).

3.3. Experiments from our group

To validate our model over various datasets, we also conducted experiments in our lab, using a CDI cell built by our group.

The electrodes were made of commercially procured activated carbon cloth (Chemviron, Zorflex FM10). Before use, the carbon electrodes were acid-washed and dried as explained elsewhere [61]. The carbon-based electrodes were characterized by Scanning Electron Microscopy (SEM) using a field emission scanning electron microscope, ZEISS, Ultra 55. Brunauer-Emmet-Teller (BET) surface area was measured by nitrogen gas adsorption employing a Micromeritics Gemini VII. Electrochemical measurements were conducted with a potentiostat/galvanostat Gamry Interface 1010E to perform Mott-Schottky analysis. A conventional three-electrode setup was used consisting of a Pt wire as the counter electrode, Ag/AgCl as reference electrode, and activated carbon cloth as the working electrode. Electrochemical impedance was measured at a fixed frequency of 100 mHz in 0.1 M NaCl within the voltage range from −0.6 to 0.9 V vs NHE. Detailed results of the material characterization are shown in Supplementary Section 6.

The CDI was assembled considering a pair of carbon electrodes cut to a size of 10 by 10 cm, and a porous cellulose-based separating film was added as a spacer, of the same size (Fig. 3). Current collectors of graphite were utilized in the device. Since the permeability of the electrodes is higher than that of the spacer, water flows through the electrode along the length of the device, meaning the CDI device has a combined flow-through and a flow-between architecture [23].

Multiple cycles of desalination/regeneration were carried out in continuous mode. The duration of the desalination and the regeneration were equal and long enough to reach the equilibrium state. The flowrate was adjusted to 10 mL/min and the applied voltage was set to 1.2 V for desalination and shorted (0 V) during regeneration. The conductivity of the effluent solution, the voltage, and the total current were automatically recorded using an online conductivity meter (EPU357 eDAQ) every second. The current and the voltage were measured using a digital multimeter Keithley 2110 and the device was automatically run over multiple cycles using a control circuit developed in-house.

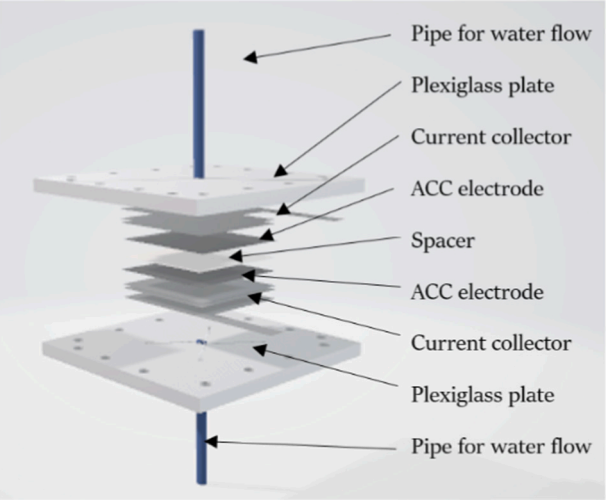

Fig. 3. An illustration of the CDI device used in our experiments. The primary components are the ACC electrode and the spacer. The inlet water enters via the pipe and a hole in the plexiglass plate to the center of the top electrode. At the outlet, the holes are at the corners of the plate, meaning the water must flow from the center to the corners before exiting the device via four tiny outlets and then converging to a single outlet pipe on the outside [23]. Because the electrodes are more permeable than the spacer, the water flows primarily through the electrodes while passing from the center inlet to the corner outlets.

4. Results

4.1. Flow-between capacitive deionization

To lay the foundations for the new studies in the later sections, this section introduces the new ELC model and relates it to the commonly used mD model. The core question here is: how well can a supercapacitor-based modeling approach simulate the CDI system?

To start let us look at the results and the data. Both the mD model and the DL-inspired formulation in the ELC model manage to accurately capture the experimentally determined equilibrium trends for charging of the supercapacitor and ion adsorption trends in the electrodes (Fig. 4a and d). The mD model provides a more detailed description of the performance for lower voltages (below 0.4 V in Fig. 4a, d), but at normal operating conditions the performance is similar. Actually, the linear-regression technique in the ELC reduces the errors somewhat, because this method is less sensitive to a non-constant capacitance.

The dynamic performance of the mD model is fair for both charging (Fig. 4b) and ion adsorption descriptions (Fig. 4c). Here, the equilibrium error has a significant impact on the differences between the experimental and simulated charge storage at the end, which stems from a non-constant capacitance of the devices in the experiments. On the other hand, the rate of charging in the ELC model also reflects the experimental conditions more closely (Fig. 4e and f). Related to this, snapshots from inside the device (Fig. 4g, h) suggest that the quicker charging (Fig. 4b) of the mD model leads to more depletion at the point of the lowest effluent concentration. Here, the improved performance of the ELC model should be attributed to an improved model framework with better implementation, rather than a more detailed physical picture. Specifically, the transparent and decoupled equation set makes it feasible to find parameter values at the fitting stage that better reflect the physical process.

The stated goal of the model as presented in the theory section was that the new model should be able to facilitate enhanced stability and straightforward implementations while obtaining at least as accurate results. Put together, this section has thus shown that the results are accurate with the new model under varying voltages, and the new modeling framework has proved to be more straightforward to implement than our implementation of the mD model.

4.2. Flow-through capacitive deionization

Another major goal in developing the model was that it should be general; that is, it should be possible to change the device structure and the model physics should still work. The previous section showed that the ELC model can replicate and enhance the simulation results for the flow-between systems. To probe the second goal, this section additionally investigates a flow-through architecture. The structure used is based on a simplified 2D model of a flat flow-through device, following a design that has also been used in other reports such as ref. [23]. Because of the lack of automatic internal boundary conditions in our mD model (from ref. [20]), we cannot compare the models side-by-side and will just show the new model.

The investigated flow-through device has a flat construction that combines the flow-through and flow-between modes, thus requiring a general description of the flow for correct modeling (Fig. 5a). The results in Fig. 5b show that there is a good fit between the simulation and the experimental effluent concentration. Notably, the stabilized implementation makes the results consistent over multiple cycles of desalination and regeneration as shown. The 2D spatial resolution makes it possible to peek inside the device during the operation. For instance, Fig. 5c shows that the potential at the beginning of the desalination process changes the most near the spacer, making the charging start at the electrode-spacer interface and move inward.

Another aspect to consider is that the model is not limited to a specific electrode structure. To illustrate the example, Fig. 5d and e shows multiple desalination cycles with electrodes coated with TiO_2 or ZnO nanoparticles respectively. Unlike the first graph in Fig. 5a, these operations used a more realistic switching procedure than always going to equilibrium. In these situations, the data shows that the experiment requires multiple cycles to settle in a stable configuration. This makes the model's ability to simulate multiple cycles imperative to finding and describing stable cycling dynamics.

Finally, the model can also predict over other quantities than the voltage that was shown previously. For instance, Fig. 5f and g shows accurate model fits and predictions for operations at different flowrates.

As a side note, the effective porosity has been investigated as a fitting parameter in previous work in the mD model [20]. Looking at the porosity parameter, a separate parameter sweep reveals that the material porosity parameter has similar effects for both the models in the flow between systems (Supplementary Fig. S1). With fewer macropores for the water to flow through (hypothetically assuming the same capacitance), the transport process of ions slows down so that it takes a longer time before the adsorption impacts the effluent concentration.

4.3. Reactions

As stated in the Goals section, we will demonstrate that the new model is tractable for new simulations that normally add a lot of instability. Having laid the foundations of the model, let us thus move on to an area in which a supercapacitor-based model has a clear strength: charge leakages. The leakages in current follow from the voltage-induced Faradaic reactions at the electrode surface, which translates to a resistive component in a circuit. This means including leakages in a simulation is straightforward and just requires an extra component in the already existing circuit model. Note that we neither distinguish between the types of reactions nor account for different reactions at the anode and cathode. The point here is to create a generalized picture. We again show only the new model because the leakage feature does not exist in our mD model.

To implement the model with leakages, we extracted the series resistance, capacitance, and leakage resistance based on a zero-dimensional Randles-fitting (Fig. 7a). Having this, the two-dimensional model uses the calculated total capacitance, distributed

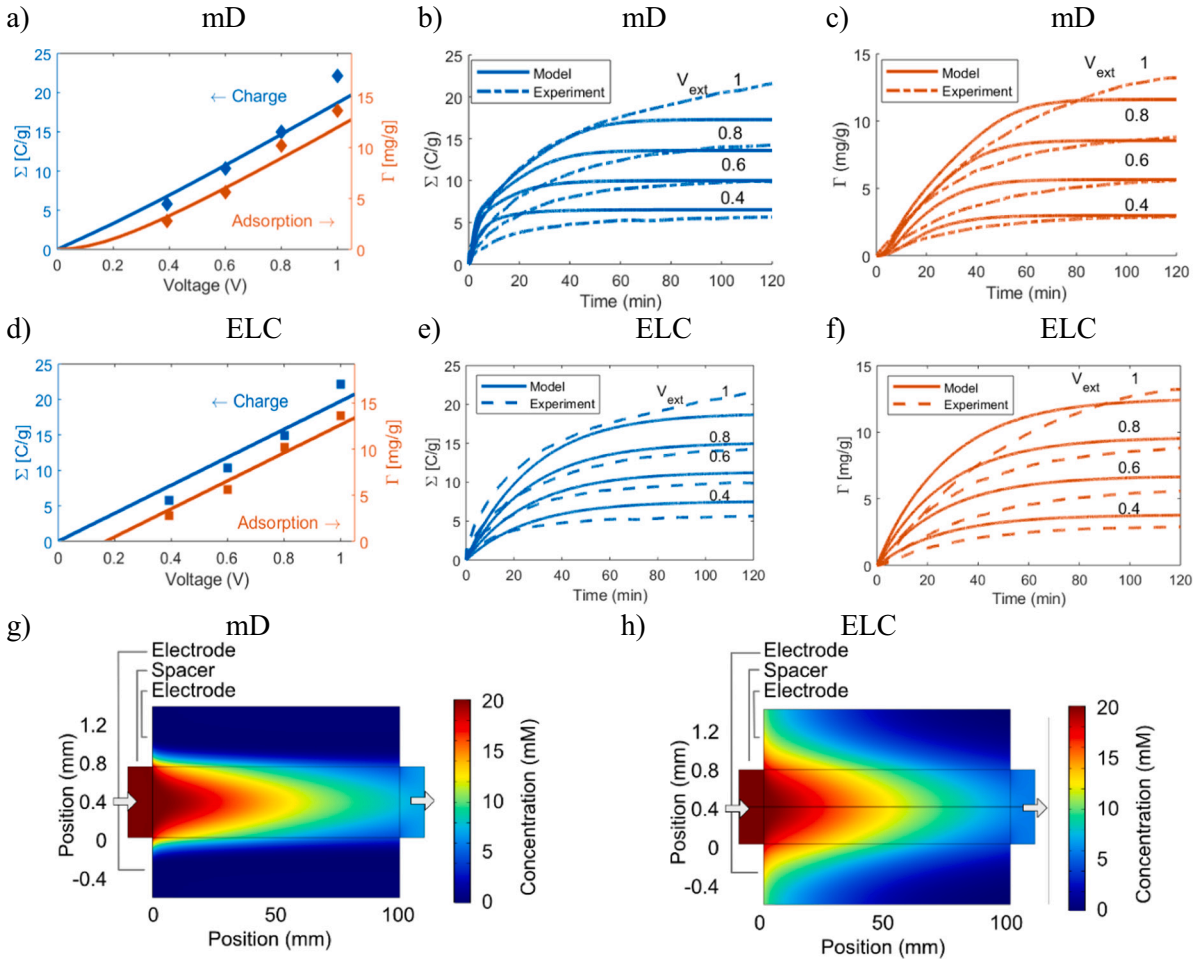

Fig. 4. Performance in a flow-between CDI device wherein solid dots and dotted lines are from experimental data and solid lines are modeling results. Experimental data were considered from ref. [20]. (a) The mD model fits the equilibrium experiment data for specific charge storage and adsorption. (b, c) The mD model predicts the dynamic experimental data for specific charge storage and adsorption, respectively. (d) The ELC model fits the equilibrium experiment data for specific charge storage and adsorption, based on the DL formulation (Eq. (16)). (e, f) The ELC model predicts the dynamic experimental data for specific charge storage and adsorption, respectively. The prediction uses the equilibrium fitting and the RC resistance in the experiment with 0.4 V applied voltage. This low voltage was chosen to separate RC contributions from the higher solution resistance that can occur substantial adsorption makes the device ion-starved. (g, h) Snapshots of the simulated internal concentration at the point of lowest effluent concentration for the mD and ELC models, respectively. The device structure uses a casing to hold the electrodes separated without a spacer material. This means almost all flow passes between the electrodes.

across the electrode surface, and the leakage resistance, across the entire electrode surface. The results show that there is excellent agreement between experimental and simulated current as functions of time (Fig. 7b). It is especially interesting to note that the model effectively and tractably simulates the Faradaic reaction with time (Fig. 7b) and as a function of the spatial location (Fig. 7c).

Interestingly, the results highlight that the leakage magnitude is the strongest at the interface between the electrode and the liquid at the beginning due to the high charging state (Fig. 7c, see also Fig. 5c). As the device charges, the leakages increase and distribute more evenly (Fig. 7d). Also, the results show several timescales of charging. Initially, the device charges on an RC timescale like a standard capacitor. Near the end, leakages dominate the process. In between, the process is a mix between the two and can also be affected by additional resistance in the solution if the concentration becomes low.

Some previous studies have argued that the Randles circuit applies to CDI [62], while a few others did not agree [63]. The key point here is that the Randles circuit is a special case of this more general theory. When the cell does not experience ion starvation, the series resistance contributes mostly to the charging rate (Eq. (1)), which means the Randles circuit works for describing the charging. When the voltage window is small, a fixed leakage resistance is a good approximation that allows the Randles circuit to describe charge leakages. Additionally, previous work has shown that the full Butler-Volmer equation predicts the leakage trends over a range of voltages, and COMSOL supports that option too [51]. Still, the advantage of being able to use the linearized version is that a leakage resistance directly and smoothly follows from the equilibrium current.

4.4. *Multi-ion formulation*

This section will further leverage the benefits of the stabilized model and investigate multi-ion solutions. We tried to implement Eq. (20) and describe multi-ion solutions with our mD model but the simulations were too unstable to converge. Therefore, this section will again look at the performance of the new ELC model with Eqs. (21)–(23).

The core model uses a circuit to calculate currents and leakages, while the stoichiometric coefficient determines how this translates to different types of ions. By knowing the time-dependent coefficient for each species, it is thus possible to simulate the ion-removal characteristic from a multi-ion solution. Numerically, the model handles this by quickly exchanging ions to maintain the correct balance (Eqs. (21)–(23)).

Fig. 8 shows the experimental results for a flow-through device

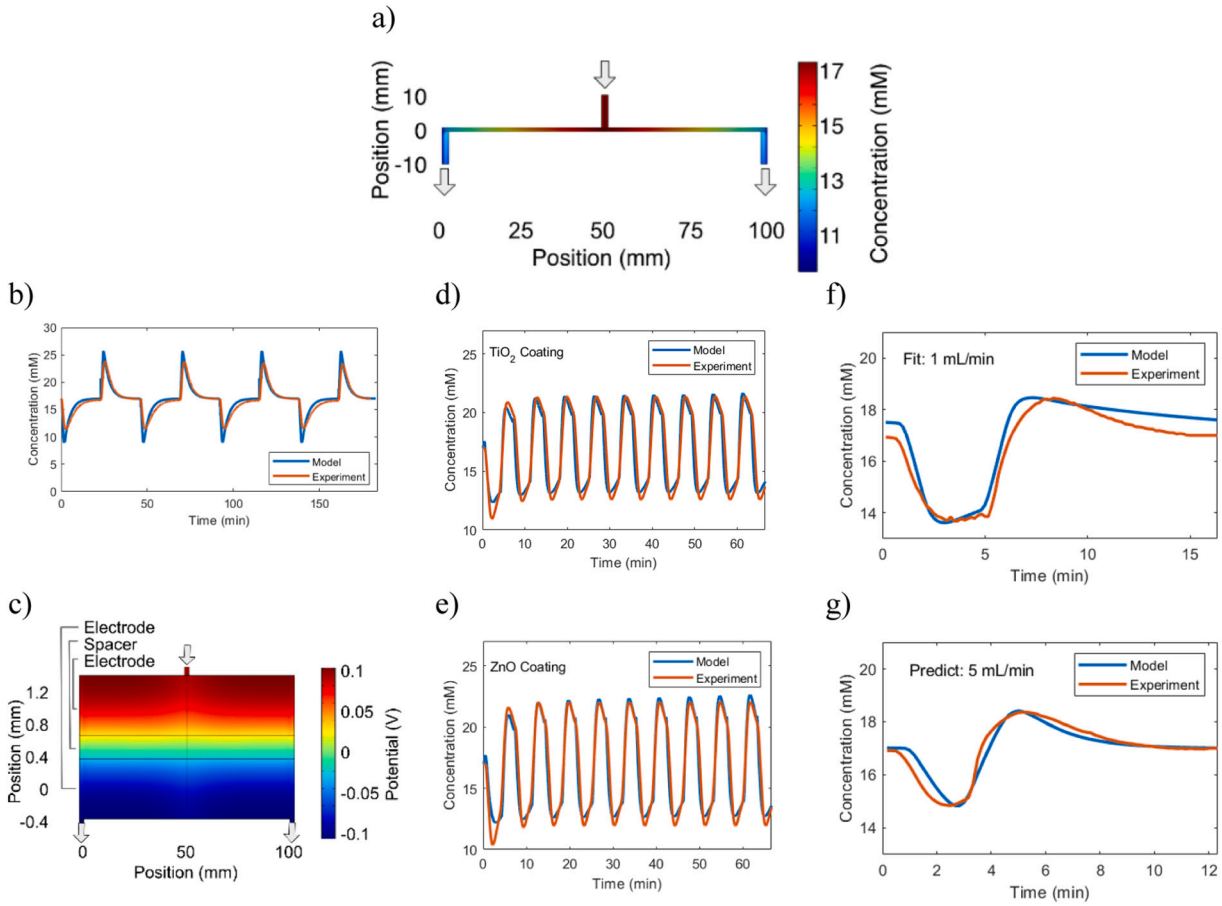

Fig. 5. Performance of a flow-through system. Experiment data for d–e from Ref. [61]. Experiment data of f–g from Ref. [46]. (a) The internal NaCl salt concentration at the point of lowest effluent concentration. (a) The effluent ion concentration for the model and experiment as functions of time, with bare ACC electrodes. (c) Potential distribution inside the device at the beginning (20 s) of the desalination operation. (d) Performance with ACC electrodes coated with TiO_2. (e) Performance with ACC electrodes coated with ZnO. (f) Model fit at 1 mL/min flowrate. (g) Prediction at 5 mL/min flowrate.

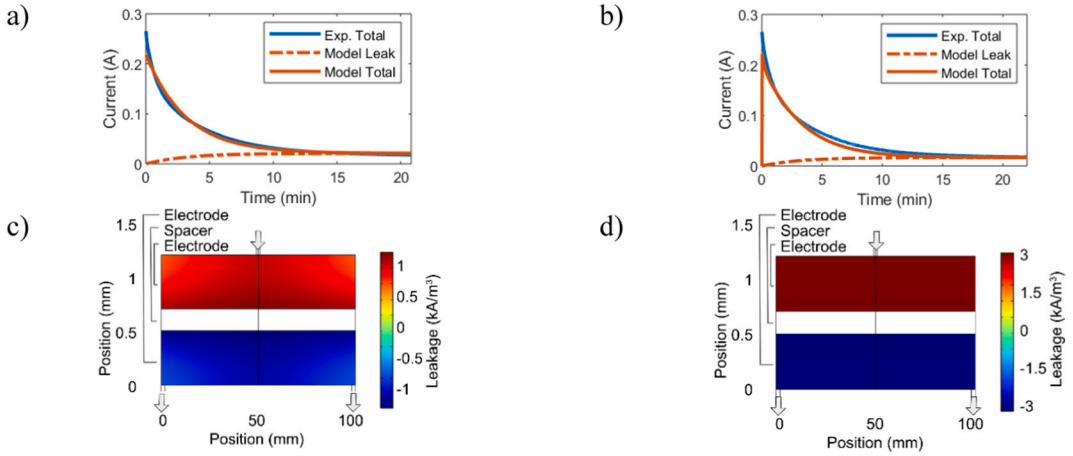

Fig. 7. Current data for the flow-through cell of Fig. 5. (a) The experimental and simulated current as functions of time, using the ELC model. The total current consists of charging current and leakage current. (b) A zoomed-in view of the spatial distribution of the charge leakages at the point of lowest effluent concentration. (c) The experimental and simulated current as functions of time, using a Randles circuit.

wherein the electrolyte containing a combination of NaCl and $CaCl_2$ was used. The experiments suggest that the device removes Na^+ and Ca^{2+} with similar rates at the beginning of the desalination process. In the end, however, the device primarily removes Ca^{2+} and even expels Na^+. This trend of higher valency ions becoming more dominant later in the process is in line with what previous studies have found [64]. Notably, the model displays the same trends, including the substitution of Na^+ for Ca^{2+}.

Based on the permeabilities of electrodes and spacer for the particular device, the model assumes that the convective flow transports ions through the electrodes rather than the spacer. This mitigates the effects of varying diffusion coefficients between species. However, the results

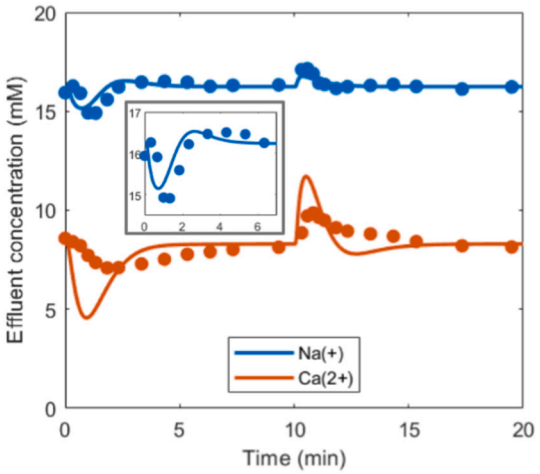

Fig. 8. Time dependent effluent concentration of Na^+ and Ca^{2+} for a flow-through desalination process wherein the electrolyte contains 1000 ppm NaCl and 1000 ppm $CaCl_2$. The dots correspond to experimental values while the lines correspond to the model results. The inset shows a zoomed-in view of the first 7 min of the effluent sodium concentration to highlight the observed ion-exchange process.

indicate that the device removes calcium faster than what simulations suggest, implying that the slower diffusion kinetics play an important role also in this system.

5. Discussion

Under what conditions are the new model valid? The model supports varying voltages and we have shown this explicitly in Fig. 4. With the current charge-efficiency formulation, we advise against simulating low voltages (less than the threshold ~0.2 V in Fig. 4). Also, note that the active reactions can be different depending on the voltage. For instance, carbon oxidation could be prominent for low voltages but voltages over the water-dissociation voltage would require a separate leakage fitting. Because of the detailed 2D formulation, the model supports varying flowrate and structures that the water flows through. All aspects related to material properties are implicit in the model parameters, so a new fitting is required for new electrode materials.

A specific condition to mention is that the implementation does not support predictions over big variations in the inlet concentrations, although the theory already exists for how to add this. Predicting over larger changes in concentration is one of the more difficult issues to be handled by any model [46,65]. Here, the challenge is that the framework of the core model is based on what was originally intended for batteries, i.e. current simulations at high ionic concentration. Currently, the model is most robust under moderate changes in medium concentrations, although it should be noted that the concentration range in which CDI behaves similarly is quite large (see Fig. 4 in ref. [38]). To properly incorporate larger variations in concentration requires a correction on the charge efficiency (see ref. [45]), the capacitance (see ref. [51]), and possibly the conductivity term (see ref. [42]).

Let us go back to the goals presented at the beginning of the theory section. These serve as an overview of the advantages of the current model relative to previous alternatives. The model was supposed to be stable, and we can see that this enables simulations of advanced features in 2D, such as leakage reactions (Fig. 7) and multi-ion solutions (Fig. 8). The reason for this stability is that the core elements, such as Eqs. (11) and (15), are decoupled and without destabilizing nonlinearities. Also, new algorithms provide more stable implementations (Eqs. (21)–(23)). Another goal was to render the model broad, general, and accurate and the results show good predictive ability (Fig. 4). It also includes simulations of both a flow-between (Fig. 4) and an asymmetric flow-through system (Fig. 5) with the same physical description.

Another of the major goals was to simplify implementation. The numerical method presented here has been developed to smoothly blend with existing libraries in COMSOL Multiphysics. Thus, it leverages the platform's extensive support for ease of implementation. This means the core formulation can be easily adapted to a variety of structures and flow modes, and the COMSOL interfaces automatically handle all transitions to the internal boundaries. Thus, there are fewer custom interfaces, which allows speedy setting up of the model and reduces human errors during the set-up. Crucially, the model also removes complex fitting schemes because the key parameters can be directly calculated.

By developing a new modeling approach, this work opens avenues for a wide arena of future studies. The integrated leakage formulation through the spatially distributed Butler-Volmer equations makes it possible to investigate Faradaic effects over a wide range of applied potentials. As an extension of these reactions, for example, we have previously seen the use of CDI devices for the production of species such chlorates [66]. Thus, it is interesting to note that knowing the charge transfer rate of specific reactions at the surface also makes it possible to investigate the production of compounds at the electrode surface of the porous electrodes that could be extended to sustainable chemical productions through electrosynthesis [67]. On the other side, the versatility and enhanced stability of the new model makes it possible to feasibly simulate complex and upscaled device structures. Another idea is to expand the current model to include the available support functions in the COMSOL platform for membrane processes to investigate membrane structures and effects in membrane CDI (MCDI).

6. Conclusions

Extensive theory exists for supercapacitors because of their immense importance in widespread applications. CDI is a desalination technique using the same type of devices, but a lot of theoretical support for CDI has evolved independently of these related advances. In this work, we develop a current-distribution approach centered on the adsorption of chemical species, the ELC model. It manages to be accurate yet adaptable to a wide range of applications because it simulates CDI in a way that blends battery-style modeling with features that are more specific to CDI operations.

Results show that the ELC model provides good prediction accuracy over varying operational conditions, such as the applied voltage. It also works for both flow-through and flow-between devices. All these simulations can reveal detailed spatiotemporal dynamics during the desalination process. We further demonstrate that the enhanced stability enables the model to tractably simulate leakage reactions as well as how they vary across time and location in the device. The model also supports time-dependent 2D simulations of multi-ion solutions, thanks to a new algorithm for describing the relative adsorption of ionic species.

There are multiple demonstrated benefits to using this model. Firstly, it is user-friendly and tractable through its adaptation to interfaces in COMSOL while retaining good simulation accuracy. Secondly, it is decoupled avoiding the common numerical issues that are experienced in 2D simulations leading to a stable computation. Indirectly, this also allows more advanced simulation studies, such as leakages and multi-ion solutions. Thirdly, the general model structure makes it widely applicable, and the same physics can be used for different device structures.

CRediT authorship contribution statement

Conceptualization, J.N. and J.D.; methodology, J.N.; software, J.N.; validation, J.N. and L.Z.; formal analysis, J.N.; investigation, J.N.; resources, J.D.; data curation, J.N, E.T, and L.Z.; writing—original draft preparation, J.N.; writing—review and editing, J.N, E.T, and J.D.; visualization, J.N.; supervision, J.D.; project administration, J.D.; funding acquisition, J.D. All authors have read and agreed to the

published version of the manuscript.

Declaration of competing interest

The authors declare that they have no known competing financial interests or personal relationships that could have appeared to influence the work reported in this paper.

Acknowledgments

The authors would like to thank the Swedish Research Council (Diary No. 2018-05387) and J. Gust. Richert Foundation (Diary No. 2020-00584) for funding the work, and the SNIC PDC supercomputing center (PDC-2020-53) for providing computing resources. Finally, J.N. sincerely thanks the support teams at COMSOL and PDC for their excellent advice and quick response times.

Appendix A. Supplementary data

The Supplementary information contains: (S-1) COMSOL model for simulating flow-between capacitive deionization. (S-2) COMSOL model for simulating flow-through capacitive deionization. (S-3) COMSOL script with dynamic parameter fitting. (S-4) COMSOL multi-ion model. (S-5) Simulations for a range of values of the microporosity. (S-6) ACC Characterization data. Supplementary data to this article can be found online at https://doi.org/10.1016/j.desal.2021.115493.

References

[1] J. Kucera, Desalination - Water From Water, John Wiley & Sons, 2014.
[2] A, S. I Water in Crisis: A Guide to the World's Fresh Water Resources, Oxford University Press, 1993.
[3] M.M. Mekonnen, A.Y. Hoekstra, Four billion people facing severe water scarcity, Sci. Adv. 2 (2016) 1–7.
[4] WWAP (United Nations World Water Assessment Programme)/UN-Water, United Nations World Water Dev. Rep. 2018 Nature-based Solut. Water, 2018.
[5] UN, Ensure access to affordable, reliable, sustainable and modern energy for all. https://sdgs.un.org/goals/goal7, 2020.
[6] UN, Ensure availability and sustainable management of water and sanitation for all. https://sdgs.un.org/goals/goal6, 2020.
[7] A. González, E. Goikolea, J.A. Barrena, R. Mysyk, Review on supercapacitors: technologies and materials, Renew. Sustain. Energy Rev. 58 (2016) 1189–1206.
[8] B.B. Sales, et al., Direct power production from a water salinity difference in a membrane-modified supercapacitor flow cell, Environ. Sci. Technol. 44 (2010) 5661–5665.
[9] D. Brogioli, F.La Mantia, Capacitive energy extraction from double layer expansion (CDLE). Fundamentals of the method, in: Interface Science And Technology 24, Elsevier Ltd., 2018, pp. 87–117.
[10] D. Brogioli, R. Zhao, P.M. Biesheuvel, A prototype cell for extracting energy from a water salinity difference by means of double layer expansion in nanoporous carbon electrodes, Energy Environ. Sci. 4 (2011) 772.
[11] R.A. Rica, et al., Electro-diffusion of ions in porous electrodes for capacitive extraction of renewable energy from salinity differences, Electrochim. Acta 92 (2013) 304–314.
[12] G.R. Iglesias, M. Ferna, Capacitive Energy Extraction From CDLE: Implementation vol. 24, Elsevier Ltd., 2018.
[13] M. Janssen, A. Härtel, R. Van Roij, Boosting capacitive blue-energy and desalination devices with waste heat, Phys. Rev. Lett. 113 (2014) 2–6.
[14] D. Brogioli, Extracting renewable energy from a salinity difference using a capacitor, Phys. Rev. Lett. 103 (2009) 31–34.
[15] Z. Jia, B. Wang, S. Song, Y. Fan, Blue energy: current technologies for sustainable power generation from water salinity gradient, Renew. Sustain. Energy Rev. 31 (2014) 91–100.
[16] S. Porada, R. Zhao, A. Van Der Wal, V. Presser, P.M. Biesheuvel, Review on the science and technology of water desalination by capacitive deionization, Prog. Mater. Sci. 58 (2013) 1388–1442.
[17] M.E. Suss, et al., Water desalination via capacitive deionization: what is it and what can we expect from it? Energy Environ. Sci. 8 (2015) 2296–2319.
[18] M.A. Anderson, A.L. Cudero, J. Palma, Capacitive deionization as an electrochemical means of saving energy and delivering clean water. Comparison to present desalination practices: will it compete? Electrochim. Acta 55 (2010) 3845–3856.
[19] T. Yu, H. Shiu, M. Lee, P. Chiueh, C. Hou, Life cycle assessment of environmental impacts and energy demand for capacitive deionization technology, Desalination 399 (2016) 53–60.
[20] A. Hemmatifar, M. Stadermann, J.G. Santiago, Two-dimensional porous electrode model for capacitive deionization, J. Phys. Chem. C 119 (2015) 24681–24694.
[21] E.N. Guyes, A.N. Shocron, A. Simanovski, P.M. Biesheuvel, M.E. Suss, A one-dimensional model for water desalination by flow-through electrode capacitive deionization, Desalination 415 (2017) 8–13.
[22] Y. Qu, et al., Charging and transport dynamics of a flow-through electrode capacitive deionization system, J. Phys. Chem. B 122 (2018) 240–249.
[23] K. Laxman, A. Husain, A. Nasser, M. Al, J. Dutta, Tailoring the pressure drop and fluid distribution of a capacitive deionization device, Desalination 449 (2019) 111–117.
[24] X. Xu, Selection of carbon electrode materials, in: Interface Science And Technology vol. 24, Elsevier, 2018, pp. 65–83 (Elsevier Ltd.).
[25] K. Laxman, M. Tay, Z. Myint, H. Bourdoucen, J. Dutta, Enhancement in ion adsorption rate and desalination efficiency in a capacitive deionization cell through improved electric field distribution using electrodes composed of activated carbon cloth coated with zinc oxide nanorods, Appl. Mater. Interfaces 6 (2014) 10113–10120.
[26] K. Laxman, M.T.Z. Myint, R. Khan, T. Pervez, J. Dutta, Improved desalination by zinc oxide nanorod induced electric field enhancement in capacitive deionization of brackish water, Desalination 359 (2015) 64–70.
[27] K. Laxman, M.T.Z. Myint, R. Khan, T. Pervez, J. Dutta, Effect of a semiconductor dielectric coating on the salt adsorption capacity of a porous electrode in a capacitive deionization cell, Electrochim. Acta 166 (2015) 329–337.
[28] M.E. Suss, et al., Impedance-based study of capacitive porous carbon electrodes with hierarchical and bimodal porosity, J. Power Sources 241 (2013) 266–273.
[29] M.E. Suss, et al., Capacitive desalination with flow-through electrodes, Energy Environ. Sci. 5 (2012) 9511.
[30] S. Porada, M. Bryjak, A. Van Der Wal, P.M. Biesheuvel, Effect of electrode thickness variation on operation of capacitive deionization, Electrochim. Acta 75 (2012) 148–156.
[31] H. Li, L. Zou, L. Pan, Z. Sun, Using graphene nano-flakes as electrodes to remove ferric ions by capacitive deionization, Sep. Purif. Technol. 75 (2010) 8–14.
[32] G. Wang, et al., Enhanced capacitance in partially exfoliated multi-walled carbon nanotubes, J. Power Sources 196 (2011) 5209–5214.
[33] H.K. Mutha, et al., Salt rejection in flow-between capacitive deionization devices, Desalination 437 (2018) 154–163.
[34] X. Gao, A. Omosebi, J. Landon, K. Liu, Enhancement of charge efficiency for a capacitive deionization cell using carbon xerogel with modified potential of zero charge, Electrochem. Commun. 39 (2014) 22–25.
[35] C. Santos, et al., Maximizing volumetric removal capacity in capacitive deionization by adjusting electrode thickness and charging mode, J. Electrochem. Soc. 165 (2018) 294–302.
[36] A. Rommerskirchen, C.J. Linnartz, D. Müller, L.K. Willenberg, M. Wessling, Energy recovery and process design in continuous flow – electrode capacitive deionization processes, Sustain. Chem. Eng. 6 (2018) 13007–13015.
[37] C. Wang, H. Song, Q. Zhang, B. Wang, A. Li, Parameter optimization based on capacitive deionization for highly efficient desalination of domestic wastewater biotreated effluent and the fouled electrode regeneration, Desalination 365 (2015) 407–415.
[38] P.M. Biesheuvel, S. Porada, M. Levi, M.Z. Bazant, Attractive forces in microporous carbon electrodes for capacitive deionization, J. Solid State Electrochem. 18 (2014) 1365–1376.
[39] O.N. Demirer, R.M. Naylor, C.A. Rios Perez, E. Wilkes, C. Hidrovo, Energetic performance optimization of a capacitive deionization system operating with transient cycles and brackish water, Desalination 314 (2013) 130–138.
[40] P.M. Biesheuvel, Activated carbon is an electron-conducting amphoteric ion adsorbent. arXiv, 2015.
[41] A. Hassanvand, G.Q. Chen, P.A. Webley, S.E. Kentish, A comparison of multicomponent electrosorption in capacitive deionization and membrane capacitive deionization, Water Res. 131 (2018) 100–109.
[42] COMSOL Multiphysics. Electrochemistry module, 2018, https://doi.org/10.1016/s1369-7021(03)00950-7.
[43] P.M. Biesheuvel, Y. Fu, M.Z. Bazant, Diffuse charge and Faradaic reactions in porous electrodes, Phys. Rev. E 83 (2011).
[44] M.E. Suss, P.M. Biesheuvel, T.F. Baumann, M. Stadermann, J.G. Santiago, In situ spatially and temporally resolved measurements of salt concentration between charging porous electrodes for desalination by capacitive deionization, Environ. Sci. Technol. 48 (2014) 2008–2015.
[45] J. Nordstrand, J. Dutta, Dynamic Langmuir model: a simpler approach to modeling capacitive deionization, J. Phys. Chem. C 123 (2019) 16479–16485.
[46] J. Nordstrand, K. Laxman, M.T.Z. Myint, J. Dutta, An easy-to-use tool for modeling the dynamics of capacitive deionization, J. Phys. Chem. A 123 (2019) 6628–6634.
[47] J. Nordstrand, J. Dutta, Simplified prediction of ion removal in capacitive deionization of multi-ion solutions, Langmuir 36 (2020) 1338–1344.
[48] J. Nordstrand, J. Dutta, Predicting and enhancing the ion selectivity in multi-ion capacitive deionization, Langmuir 36 (2020) 8476–8484.
[49] J. Nordstrand, J. Dutta, Basis and prospects of combining electroadsorption modeling approaches for capacitive deionization, Physics (College. Park. Md) 2 (2020) 309–324.
[50] J. Nordstrand, J. Dutta, Design principles for enhanced up-scaling of flow-through capacitive deionization for water desalination, Desalination 500 (2020), 114842.
[51] J. Nordstrand, D. Joydeep, An extended randles circuit and a systematic model-development approach for capacitive deionization (doi:Communicated), J. Electrochem. Soc. 2020 (2020).
[52] J. Nordstrand, J. Dutta, Flexible modeling and control of capacitive-deionization processes through a linear-state-space dynamic-Langmuir model, npj CleanWater 4 (2021) 1–7.

[53] J.E. Dykstra, R. Zhao, P.M. Biesheuvel, A.Van Der Wal, Resistance identification and rational process design in capacitive deionization, Water Res. 88 (2016) 358–370.
[54] G. Dongowski, R.H.H. Neubert, L. Heinevetter, Permeation of bile acids across artificial lipid membranes and caco-2 monolayers, Pharmazie 54 (1999) 517–520.
[55] G.J. Brug, A.L.G. van den Eeden, M. Sluyters-Rehbach, J.H. Sluyters, The analysis of electrode impedances complicated by the presence of a constant phase element, J. Electroanal. Chem. 176 (1984) 275–295.
[56] S. Porada, et al., Direct prediction of the desalination performance of porous carbon electrodes for capacitive deionization, Energy Environ. Sci. 6 (2013) 3700–3712.
[57] P.M. Biesheuvel, M.Z. Bazant, Nonlinear dynamics of capacitive charging and desalination by porous electrodes, Phys.Rev. E Stat. Nonlinear Soft Matter Phys. 81 (2010) 1–12.
[58] P.M. Biesheuvel, R. Zhao, S. Porada, A. van der Wal, Theory of membrane capacitive deionization including the effect of the electrode pore space, J. Colloid Interface Sci. 360 (2011) 239–248.
[59] C.A.R. Perez, O.N. Demirer, R.L. Clifton, R.M. Naylor, C.H. Hidrovo, Macro analysis of the electro-adsorption process in low concentration NaCl solutions for water desalination applications, J. Electrochem. Soc. 160 (2013) E13–E21.
[60] J. Nordstrand, D. Joydeep, Relaxed adsorption-flow coupling enables stable COMSOL Multiphysics® modeling of upscaled capacitive deionization, in: COMSOL Conference 2020 Grenoble, COMSOL, 2020.
[61] K. Laxman, D. Kimoto, A. Sahakyan, J. Dutta, Nanoparticulate dielectric overlayer for enhanced electric fields in a capacitive deionization device, ACS Appl. Mater. Interfaces 10 (2018) 5941–5948.
[62] M. Qin, A. Deshmukh, R. Epsztein, S.K. Patel, Comparison of energy consumption in desalination by capacitive deionization and reverse osmosis, Desalination 455 (2019) 100–114.
[63] A. Ramachandran, et al., Comments on "Comparison of energy consumption in desalination by capacitive deionization and reverse osmosis", Desalination 461 (2019) 30–36.
[64] R. Zhao, et al., Time-dependent ion selectivity in capacitive charging of porous electrodes, J. Colloid Interface Sci. 384 (2012) 38–44.
[65] J. Nordstrand, J. Dutta, A new automated model brings stability to finite-element simulations of capacitive deionization, Nano Sel. 1–15 (2021), https://doi.org/10.1002/nano.202100270.
[66] M.I. Alvarado Ávila, E. Toledo-Carrillo, J. Dutta, Improved chlorate production with platinum nanoparticles deposited on fluorinated activated carbon cloth electrodes, Clean. Eng. Technol. 1 (2020), 100016.
[67] Y. Yuan, A. Lei, Is electrosynthesis always green and advantageous compared to traditional methods? Nat. Commun. 11 (2020) 2018–2020.